

A Computational Study Using Time Reversal Focusing for Hyperthermia Treatment Planning

Pegah Takook*, Hana D. Trefná, Xuezhi Zeng, Andreas Fhager, and Mikael Persson

Abstract—In hyperthermia treatment planning (HTP) the goal is to find the amplitudes and phases of antennas in the applicator to efficiently heat the tumor. To do this prior information regarding tumor characteristics such as the size, position and geometry, in addition to an exact model of the hyperthermia applicator is needed. Based on this information, the optimal frequency of operation can be determined. In this paper the optimum frequency for hyperthermia treatment based on the tumor and applicator characteristics, using time reversal as the focusing technique, is studied. As prior information, we consider tumor size and position, the number of the antennas in the applicator and the frequency characteristics. The obtained optimal frequency range is found using hyperthermia quality indicator values calculated from simulations. We also determine the optimum position of the virtual source in the initial step of the time reversal method to increase the quality of the treatment.

1. INTRODUCTION

In the last two decades studies have shown the benefits of adding hyperthermia to radiotherapy to treat many types of tumors [1, 2]. The goal of hyperthermia treatment is to heat tumors to therapeutic temperatures of 39–44°C, while keeping the temperature in healthy tissues below critical values. The goal of the hyperthermia treatment planning process is to find a set of treatment parameters that maximizes treatment quality. It has been well established that this quality has a direct impact on the improvement of treatment outcome [3, 4].

Phased arrays are the most common hyperthermia applicators to heat deep-seated tumors. They utilize the constructive wave interference from a set of antennas at the tumor site [5–8]. The parameters that determine the system’s ability to focus are the phases and amplitudes of the excitation of antennas in the phased array. The optimal values of these settings, result in optimal tumor heating with acceptable heating of the surrounding tissues. These optimal settings are often sought by maximizing a specific absorption rate (SAR), which is defined as the rate at which energy is absorbed by the human body [13, 14]. SAR is driving the temperature which in turn is smeared out by perfusion and diffusion.

Previously we proposed a new focusing technique based on the time-reversal cavity principle for hyperthermia treatment planning [9]. This method which makes use of the time-symmetry characteristics of the wave equation even in a strongly heterogeneous medium, has good focusing ability and is excellent for focusing through complex media. The method is divided into two parts. In the first part, using finite-difference time-domain (FDTD) modeling, the radiated waves from a point-like source are detected by the model of the antenna system. As the point-like source is placed into the tumor only in this numerical step, we use the term ‘virtual source’ thorough the paper. The detected signals are then driving antennas in a time-reversed order in a real system. However in this paper the second part is also modeled using the FDTD method. Unlike traditional optimization methods, in using the time reversal focusing there is no need to calculate the electric field of each individual antenna in the phased

Received 16 November 2016, Accepted 17 March 2017, Scheduled 24 March 2017

* Corresponding author: Pegah Takook (pegaht@chalmers.se).

The authors are with the Department of Signals and Systems, Chalmers University of Technology, Göteborg, Sweden.

array. Moreover the time reversal has the flexibility to work with ultra-wideband signals with ability to decrease hot spots thus improving the SAR distribution in the treated area [10]. Nevertheless, a similar effect can be achieved by sweeping among a number of frequencies within the operational frequency band during the treatment, referred here as a multi-frequency approach.

In our previous study, a 2D implementation of the time reversal method was used for hyperthermia treatment planning [9]. Although some limiting factors of the 2D algorithm prevented us to fully discover the efficacy of the focusing method, basic information about the feasibility and performance of the time reversal were given. Further, we validated the feasibility and accuracy of the time reversal treatment planning experimentally with our UWB hyperthermia system [11]. The results showed an excellent agreement between the simulated and experimental data, in terms of thermal profiles obtained in homogeneous muscle phantom [12]. The goal of this study, which extend our previous numerical work, is to speed up the treatment planning process for the multi-frequency approach by having a prior knowledge of the appropriate frequency range and the optimum virtual source position. We employ the time reversal to find the optimum frequency of operation for a specific tumor size and position. Further, we study an ideal positioning of the virtual source in the first step of the time reversal to achieve the foremost tumor coverage.

The paper is structured as follows. In Section 2 we review the principle of the FDTD time reversal algorithm and present the numerical tumor models used in this study. We also introduce quality indicators for evaluating the performance of the time reversal method. In Section 3, the 2D time reversal analysis results are presented in terms of the optimum frequency given tumor position, size and the number of antennas in the hyperthermia applicator. Later, the optimum position of the virtual source for a specific tumor is found using 3D time reversal. Analysis of realistic tumor models is presented, and the dependence of treatment outcome versus the frequency and position of the virtual source are discussed.

2. METHODOLOGY

2.1. Time Reversal for Hyperthermia

We here describe the basic principle of the time reversal focusing method for microwave hyperthermia. A point-like source, so called virtual source, located inside a numerical human model with a known tumor location, initially generates spherical wavefronts which are distorted after propagation through the inhomogeneous medium, Figure 1(a). The electric fields on the surface of the model are then recorded from the numerical simulations. In a second step the initial source is removed and the time reversed signals are used to drive the antenna elements on the surface of the model. As it is shown in Figure 1(b), the back-propagated time-reversed electric fields are focused at the original position of the virtual source. In using the time reversal in a real system, this second step is performed driving the real antennas.

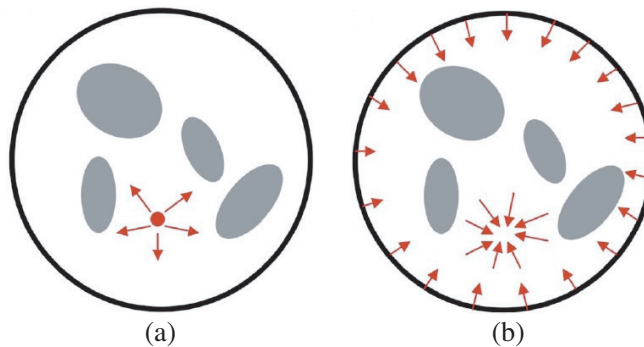


Figure 1. The principle of the time-reversal method. (a) The recording step with virtual source in the target location. (b) The time-reversed step.

2.2. Electromagnetic Modeling and Evaluation

2.2.1. Plane Wave Modeling

We first consider a simplified case with two plane waves propagating in $+y$ and $-y$ directions and described by E_z^1 and E_z^2 , respectively. If the plane waves at $y = \pm L/2$ have amplitudes A_1 and A_2 and phases ϕ_1 and ϕ_2 , respectively, then the total electric field at any point along y -axis is

$$E_z(y) = E_z^1 + E_z^2 = A_1 e^{+j\phi_1} e^{-\gamma(y+L/2)} + A_2 e^{+j\phi_2} e^{\gamma(y-L/2)} \quad (1)$$

where $\gamma = \alpha + j\beta$ is the propagation constant, α the attenuation constant (Np/m) and β the phase constant (rad/m). The power density as a function of position is then given by:

$$P(y) = \frac{\sigma}{2} E_z^*(y) E_z(y) = \frac{\sigma}{2} \left(A_1^2 e^{-2\alpha(y+L/2)} + A_2^2 e^{2\alpha(y-L/2)} + 2A_1 A_2 e^{-\alpha L} \cos(-2\beta y + \phi_1 - \phi_2) \right) \quad (2)$$

Analogously, the power density can be derived for more plane waves. In our study, we include the results for 4 and 8 plane waves located equidistantly on a circular phantom of radius 100 mm. Considering equal amplitudes and phases for all the plane waves, the constructive wave interference is obtained in the center of the phantom, at the origin, i.e., $y = 0$ and $x = 0$. The dielectric properties of the phantom were considered the same as the background material.

2.2.2. 2D Modeling

A 2D numerical analysis is carried out using a circular muscle phantom with a radius of 100 mm, surrounded by water. The antennas are modeled as hard sources and are placed 15 mm apart from the phantom surface as shown in Figure 2. The same figure also shows the tumor center position, TCP, which is defined as the tumor center distance to the phantom center. The number of antennas is varied from 4 to 48. The amplitude and phase settings of the antennas are calculated to focus in different positions along the axis of the phantom using the time-reversal method. Power absorption values are calculated for single frequencies σ in the frequency range of 400–900 MHz.

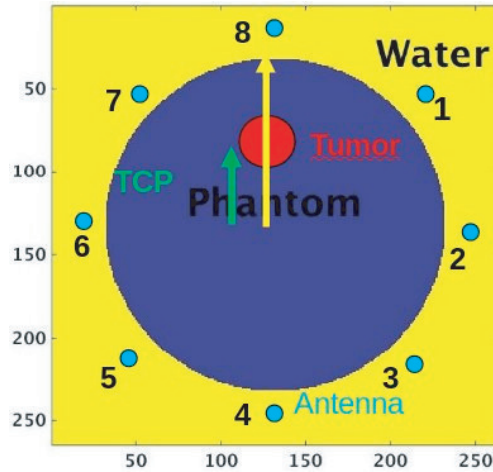


Figure 2. Set-up of 2D simulations in FDTD-based code shows a cylindrical phantom surrounded by water.

2.2.3. 3D Modeling

In order to evaluate the results from the 2D-analysis in more realistic scenarios, we perform three-dimensional (3D) simulations to calculate power deposition inside the numerical model of a head and neck (H&N) phantom. The phantom includes seven anatomical structures and its numerical model is derived from segmented computed tomography (CT) data of the phantom. Realistic tumor model is inserted in base of the tongue. The simulations were performed in an in-house-developed FDTD based

code as well as in commercial package CST Microwave Studio 2014 (CST, Darmstadt, Germany) [15], including a detailed model of the antenna array system [16]. Figure 3(a) shows the transverse plane through the tumor center. The tongue tumor has an approximate radius of 16 mm. The dielectric properties of the phantom tissues are calculated using the Cole-Cole parameters of Gabriel et al. [17], while the dielectric properties of the tumor are calculated using the parametric model proposed by Lazebnik et al. [18]. We use the Cole-Cole parameters of their curve corresponding to the 75th percentile of the cancer samples containing 30% or more malignant tissue content. Note that the Lazebnik parameters are for breast tumors but we use them as an approximation in our head and neck analysis. Table 1 exemplifies the derived dielectric properties at 500 MHz.

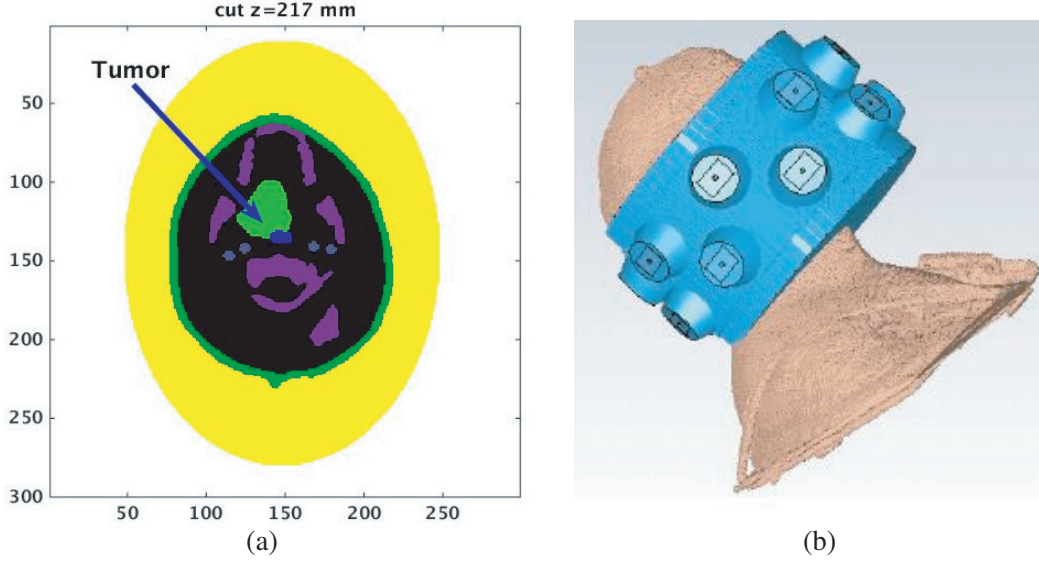


Figure 3. (a) The transverse plane of the tongue tumor model. The tumor is represented in green color. (b) The antenna applicator for the head.

Table 1. The exemplified dielectric properties of the phantom tissues at 500 MHz.

Tissues	ϵ	$\sigma[S/m]$	Mass density [kg/m^3]
Air-Exterior	1	0	1.293
Muscle-Phantom	56.9	0.82	1.04e3
Bone	12.93	0.099	1.99e3
PEC	1	6e7	8.93e3
Skin	44.9	0.723	1.12e3
Eyes	68.9	1.54	1.00e3
Blood	63.9	1.38	1.04e3
Tumor	56.8	0.51	1.05e3
Trachea	43.4	0.65	1.08e3
Water bolus	83.8	0.086	1.00e3

The applicator used in this study is developed for treatment of head tumors, Figure 3(b). It consists of 16 antennas arranged in two-rings. The applicator has elliptical shape with major and minor radii 135 and 100 mm along y - and x -axis, respectively. The tumor is placed in the center of the applicator. The antenna elements in the applicator are Bow-Tie antennas operating in a wide-band frequency range of 430–900 MHz. Each of the antennas are immersed in a water bolus with the shape of truncated cone. They are placed on a second layer of water bolus with a thickness of approximately 2 cm, which is placed

in turn around the head. The role of water bolus in hyperthermia is twofold; to improve the impedance matching between the antennas and the body and to cool the surface of the body.

2.3. Performance Indicators

The quality of hyperthermia treatment is strongly dependent on the amount of energy absorbed in the tumor and in the surrounding healthy tissues. High SAR values in the target region results in higher temperatures which are paramount for good treatment outcome. On the other hand, peaks of SAR in healthy tissues, called hotspots, are detrimental to the treatment quality. Hotspots restrict the total applied power as they may cause damage, as well as pain, to the healthy tissues and therefore need to be minimized.

The performance of the treatment plan is assessed by appropriate quality indicators providing quantitative information of energy absorbed in the tumor as well as in the healthy tissues. The first indicator, the average power absorption ratio (aPA), is used to quantify the relative amount of energy that is absorbed in the tumor. It is defined as the ratio between the average power absorption in the tumor volume V_{tum} and the average power absorption in the remaining tissue V_{rt} [9]:

$$aPA = \frac{\frac{1}{N_{V_{\text{tum}}}} \sum^{V_{\text{tum}}} PA}{\frac{1}{N_{V_{\text{rt}}}} \sum^{V_{\text{rt}}} PA} \quad (3)$$

where $N_{V_{\text{tum}}}$ and $N_{V_{\text{rt}}}$ are the total number of voxels of the tumor and non-tumor tissues, respectively. The other quality indicator, used to quantify peak power absorption values in healthy tissues with respect to the median PA in the tumor, is RTMi or remaining tissue maximum index:

$$RTMi = \frac{PA_1(\text{remaining tissue})}{PA_{50}(\text{tumor})} \quad (4)$$

with PA_1 as the value indicating the highest percentile of the power absorption in the healthy tissue and PA_{50} as the median power absorption in the tumor. These two quality indicators are mostly useful to show the heating ability of the applicator, where high aPA and low RTMi values are desired.

Yet another performance indicator is highly relevant for the analysis. The target coverage 25% ($TC_{25\%}$), which indicates the homogeneity of the absorbed energy in the tumor. This is defined as the percentage of tumor volume covered by 25% of the maximum SAR in the whole patient model. While we use this indicator to evaluate the performance of 3D analyses, we define target coverage 50% to evaluate 2D analyses. Similar to $TC_{25\%}$, $TC_{50\%}$ is defined as the percentage of tumor volume covered by 50% of the maximum SAR of whole patient model [19].

3. RESULTS

In the following section we present numerical results of the studies discussed above to determine the most favorable operational settings. In the first series of calculations, we investigate the effect of the number of radiating elements, tumor positions and tumor sizes on the optimal frequency. In the next step, we present results of the optimal position of the virtual source that gives the best treatment outcome.

3.1. The Impact of Frequency and Number of Antennas on Focusing Abilities

3.1.1. Plane Wave Analysis

As discussed in the previous section, we first consider our radiating sources as plane waves. Using the obtained analytical power loss densities for 2, 4 and 8 plane waves, we can study the effect of the number of plane waves and frequency on aPA. For 2 plane waves we have a 1D problem and for the rest we have to solve a 2D problem. Figure 4 shows the calculated aPA in a tumor of radius 10 mm at the origin. The aPA is plotted for 2, 4 and 8 plane waves at different frequencies. As is shown in Figure 4,

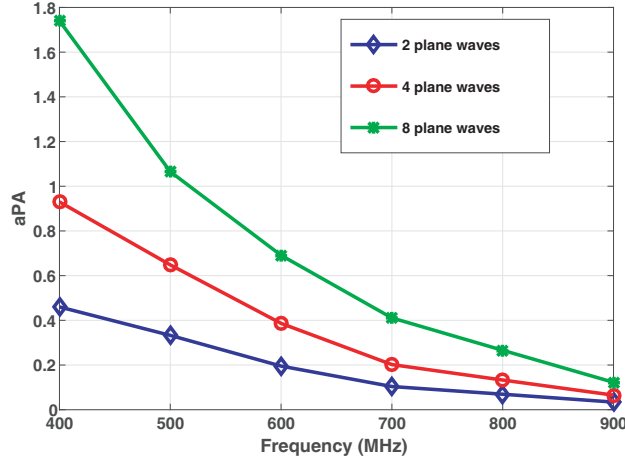


Figure 4. Computed aPA at tumor from 2, 4 and 8 radiating plane waves.

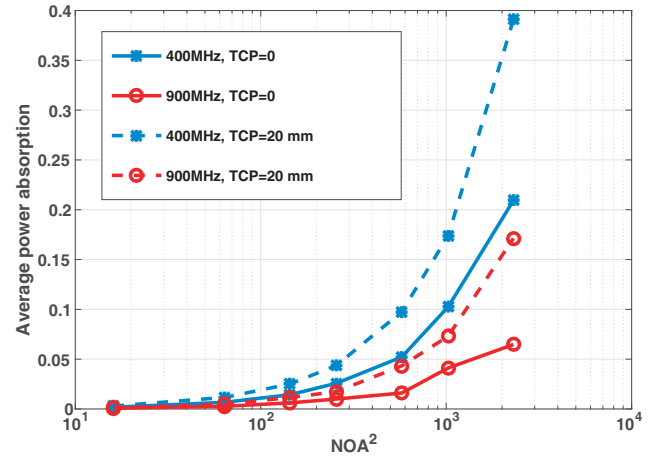


Figure 5. Average power absorption in a tumor of radius 1 mm located at phantom center (TCP = 0) and 20 mm to the phantom center (TCP = 20 mm) versus NOA^2 (number of antennas squared).

as the frequency is increased the value of aPA is decreased for 2, 4 and 8 number of plane waves. At the lowest frequency 400 MHz, difference between the aPA values for different number of plane waves is the highest. As the frequency is increased, this difference is getting negligible such that aPA values for 2, 4 and 8 number of plane waves are converging.

3.1.2. 2D Modeling

In the next step, the simulations were performed using a FDTD-based, in-house developed code. The set-up of the simulations were similar to the simple analytical case discussed above. A circular phantom with radius of 100 mm was surrounded with water and the antennas were placed 15 mm away from the phantom surface, Figure 2. Using the time reversal method, amplitudes and phases at all the antennas were calculated and used to focus in tumor. This was done for different tumor positions along the axis of the phantom. Using these amplitudes and phases in a time reversed order, the average power absorption values in the tumor were calculated in the frequency range of 400–900 MHz. The antennas were modeled as hard sources and the number of antennas were increased from 4 to 48.

In Figure 5, the average power loss absorption in a tumor of radius 1 mm is plotted versus number of antennas squared, (NOA^2). The tumor center was first located in the phantom center, TCP = 0, and then 20 mm from the phantom center, TCP = 20 mm. As we increase the number of antennas, higher power is absorbed for both tumor positions. However, for tumor positioned away from the center, the performance improves more with the number of antennas than for the tumor in the middle. This shows that heating a deep seated tumor is a more challenging task.

In Figure 6, more detailed results are presented of the power absorption distribution in the tumor versus the size and position of the tumor, the frequency and the number of antennas. In these results, the average power absorption ratio was computed for 7 tumor positions along the axis of the phantom in Figure 2(a). The computation was performed for frequencies in the range of 400–900 MHz and the number of antennas was changed from 4 to 48. Iso-surfaces for 6 different aPA values were extracted and plotted in the space of the number of antennas (NOA), tumor position and frequency. The tumor position is measured in terms of the distance of the tumor center from the phantom center. As is shown in Figure 6, the iso-surface with the highest aPA = 30 is the smallest surface obtained for highest number of antennas, largest tumor position and highest frequencies. The surface for aPA = 5 covers the tumor positions between 20–70, all frequencies between 400–900 MHz and all number of antennas between 4–48. For each tumor position and at a specific frequency, the highest values of aPA were obtained for 48 antennas. While the presented results were obtained for a tumor radius of 10 mm, similar results were obtained for tumor radii of 7.5 mm and 15 mm.

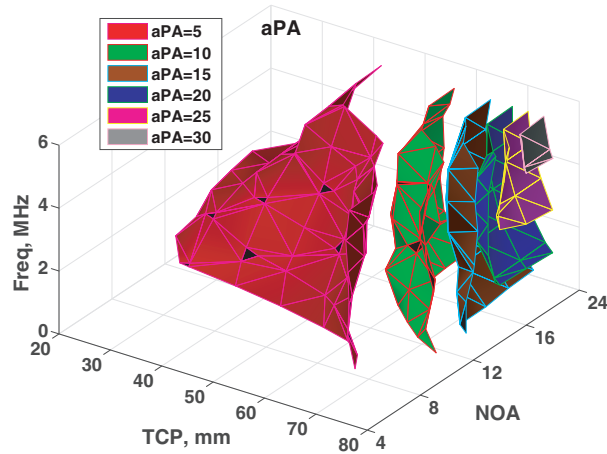


Figure 6. Iso surf plot of the aPA versus frequency, number of antennas and tumor center distance to the phantom center.

In Figure 7, 50% tumor coverage is plotted versus the tumor position at different frequencies. Different number of antennas are used and the tumor radius is 10 mm. For the lowest frequency of 400 MHz, more than 80% tumor coverage was obtained for all tumor positions and all number of antennas, except for 4 antennas. By increasing the frequency, the 50% tumor coverage dropped for the lower number of antennas and for deep-seated tumors. 50% tumor coverage was zero at 900 MHz for a deep seated tumor if the number of antennas is greater than or equal to 24.

Based on the results in Figures 6 and 7, we obtain the optimum performance in terms of frequency range for which we have the highest aPA while we have around 75% tumor coverage. The obtained results are shown in Table 2, where we show tumor positions normalized to the phantom radius and call it the tumor position ratio, TPR. For $TPR < 0.3$, the highest aPA was in the frequency range of 400–500 MHz, with the highest aPA obtained close to the lower bound of 400 MHz. The same frequency range was also optimal for $0.3 \leq TPR < 0.5$ with the highest aPA close to 500 MHz when the number of antennas is greater than or equal to 16 and the highest aPA close to 400 MHz when number of antennas is less than or equal to 16. For superficial tumor positions with $0.5 \leq TPR$, the lower and upper bound of the optimal frequency range was increased by increasing the number of antennas from 16.

Table 2. The selected frequencies versus the tumor position and the number of antennas.

	NOA = 8	NOA = 12	NOA = 16
TPR > 0.8	$400 < F \leq 500$ MHz	$400 \leq F < 500$ MHz	$400 < F \leq 500$ MHz
$0.5 \leq TPR \leq 0.8$	$400 \leq F < 500$ MHz	$400 \leq F < 500$ MHz	$400 < F \leq 500$ MHz
$0.3 \leq TPR < 0.5$	$F \leq 400$ MHz	$400 \leq F < 500$ MHz	$400 < F \leq 500$ MHz
TPR < 0.3	$F \leq 400$ MHz	$400 \leq F < 500$ MHz	$400 \leq F < 500$ MHz
	NOA = 24	NOA ≥ 32	-
TPR > 0.8	$600 < F \leq 700$ MHz	$700 < F \leq 800$ MHz	-
$0.5 \leq TPR \leq 0.8$	$600 < F \leq 700$ MHz	$700 < F \leq 800$ MHz	-
$0.3 \leq TPR < 0.5$	$400 < F \leq 500$ MHz	$400 < F \leq 500$ MHz	-
TPR < 0.3	$400 \leq F < 500$ MHz	$400 \leq F < 500$ MHz	-

From the results presented above we can see that heating of deep seated tumors is challenging. This is not surprising but it is interesting to see how the size of the tumor affects the obtained aPA and tumor coverage. In Figure 8 we computed the aPA and 50% tumor coverage for a tumor in center of the phantom with 48 antennas while changing the frequency and the tumor radius. We then found

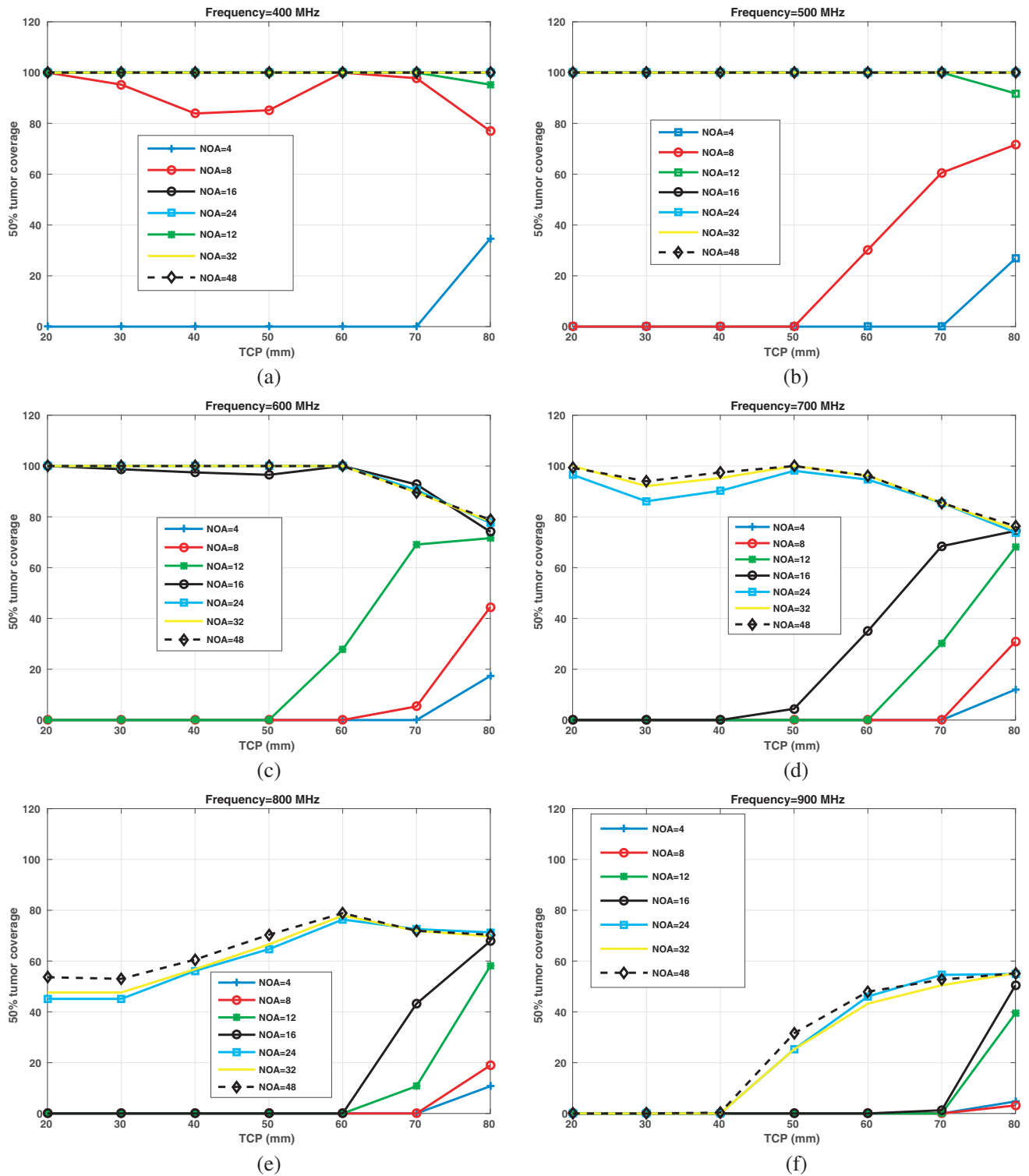


Figure 7. 50% tumor coverage as a function of tumor center position (TCP) for different number of antennas at (a) 400 MHz, (b) 500 MHz, (c) 600 MHz, (d) 700 MHz, (e) 800 MHz and (f) 900 MHz. The tumor radius is 10 mm. The number of antennas is shown with NOA.

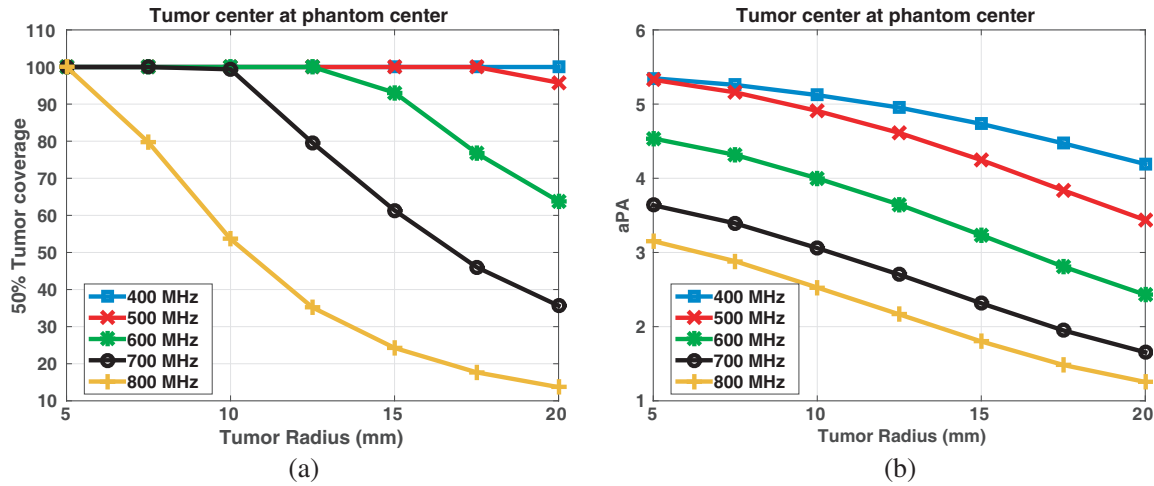


Figure 8. (a) 50% tumor coverage and (b) aPA versus tumor size, for 48 number of antennas when tumor center is in the phantom center.

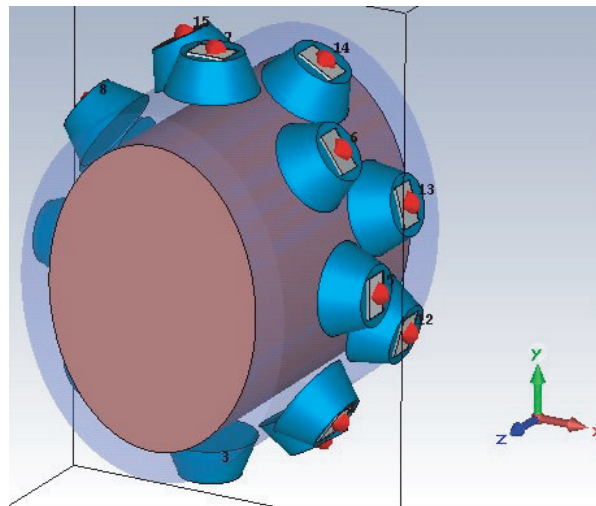


Figure 9. Homogeneous muscle phantom inside an array of 16 bow-ties used for sensitivity analysis of virtual source position.

that, more than 75% tumor coverage can be achieved up to 700 MHz when the tumor radius ≤ 13 mm. This corresponds to aPA value of approximately 2.5. For a tumor radius of 20 mm, frequencies up to 500 MHz resulted in about 96% tumor coverage which corresponds to an aPA of 3.44.

3.2. Analysis of 3D Modeling

3.2.1. Virtual Source Placement

Another free parameter in optimizing the treatment planning is the position of virtual source. For this purpose, we performed a study of the most appropriate position of the virtual source given the tumor size and position and the frequency. Spherical tumors of different radii positioned along the major axis of a homogeneous elliptical muscle phantom. The muscle phantom was surrounded by a single water bolus and 16 bow-tie antennas immersed in separate conical shape water containers. Figure 9 shows the phantom with a major radius of 100 mm and minor radius of 73 mm. Two homogeneous tumors were considered with radii 10 mm and 16 mm. For each tumor position, we changed the position of the

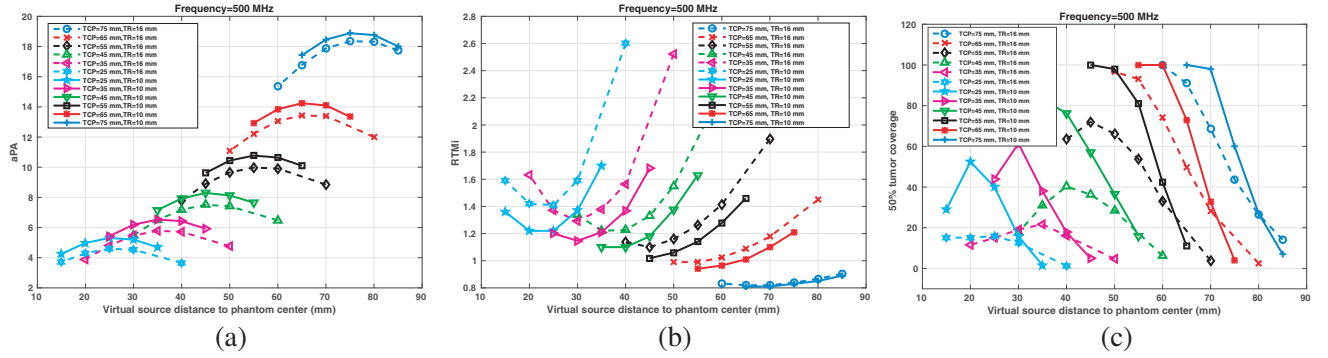


Figure 10. (a) aPA (b) RTMi and (c) $TC_{50\%}$ versus virtual source positions at 500 MHz. In all plots solid lines show tumor radius 10 mm and dash lines show tumor radius 16 mm.

virtual source along the major axis of the tumor model. The amplitudes and phases of the antennas were found using the time reversal method for each virtual source position. By computing the power absorption values inside and outside of the tumor, we studied the effect of virtual source positions on aPA, RTMi and $TC_{50\%}$ for 4 different frequencies 400, 500, 700 and 900 MHz.

Figure 10 shows the computed aPA, RTMi and target coverage 50% for six tumor positions with radii 10 and 16 mm at 500 MHz. Here aPA, RTMi and target coverage are plotted versus the distance between the virtual source and the phantom center. For each tumor position, five virtual source positions along the major axis of the phantom were considered. As shown in Figure 10(a), maximum power absorption was obtained when the virtual source was located in the center of the tumor. However, Figure 10(b) shows that results for RTMi are not that simple. For tumor radius 10 mm and $TCP \geq 45$ mm, the lowest RTMi value was obtained with the virtual source closest to the phantom center. For centrally located tumors, the virtual source position closer to the tumor center gives a lower RTMi.

In Figure 10(c), the highest 50% target coverage for each tumor position is obtained at the virtual source closest to the phantom center when $TCP \geq 45$ mm, while for more deep-seated tumors, the virtual source positions closer to the tumor center are optimal. The conclusion for a 10 mm tumor radius holds also for a 16 mm tumor radius.

We then extended the study to investigate the frequency dependence of the results. Figure 11 shows the computed tumor coverage for 400, 700 and 900 MHz plotted for different virtual source positions along the phantom major axis. Figure 11(a) shows that for 400 MHz and $TCP \geq 55$ mm the optimum virtual source is outside of the tumor, toward the phantom center. As the tumor is moved toward the phantom center, ($TCP < 55$ mm), the optimum virtual source gets closer to the tumor center. However, for 700 MHz, as the tumor is moved toward the phantom center, the optimum virtual source moves toward the phantom surface, see Figure 11(b). At 900 MHz, the 50% tumor coverage is only obtained for the most superficial tumor position. Although the optimum virtual source in this case is close to the phantom surface, the 50% tumor coverage is minimal, see Figure 11(c).

Based on these results we calculate the virtual source displacement from the tumor center to the position where maximum tumor coverage was achieved, TC_{max} , for tumor radii 10 and 16 mm. The virtual source displacement is taken to be positive in the direction toward the phantom center, or $-y$ axis. As shown in Figure 12, the general trend is that, as the tumor moves toward the boundary of phantom, the optimum virtual source is moving toward the phantom center. Moreover, for tumors close to the phantom boundary 100% tumor coverage can be obtained at both 400 and 500 MHz.

3.2.2. Virtual Source Placement in a Realistic Tumor Model

To find the optimum position of the virtual source in realistic inhomogeneous tumors, we performed a study of the tongue tumor described previously in Section 2.2.3. The applicator used for this simulation is the head applicator with 16 antennas shown in Figure 3. In the simulations, an extra water bag

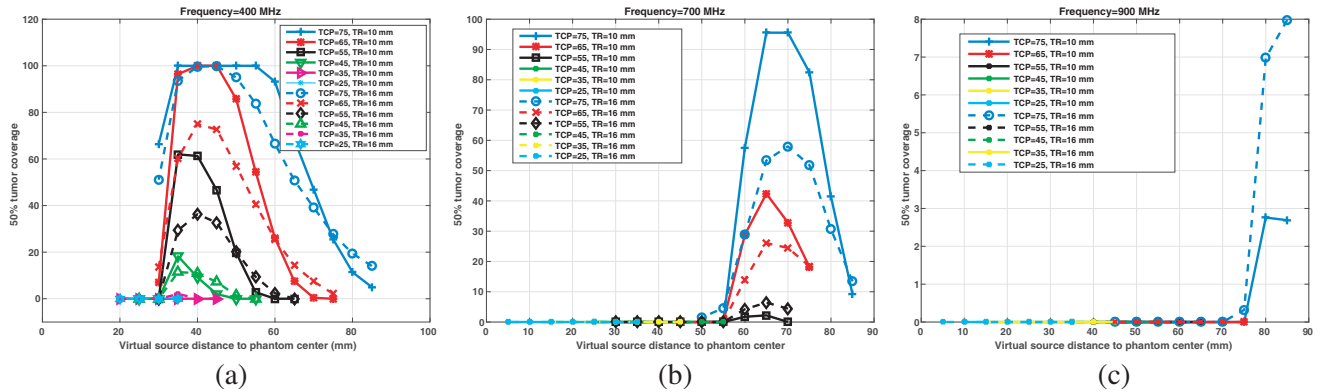


Figure 11. (a) $TC_{50\%}$ versus virtual source positions at 400 MHz (b) $TC_{25\%}$ versus virtual source positions at 700 MHz (c) $TC_{25\%}$ versus virtual source positions at 900 MHz. In all plots solid lines show tumor radius 10 mm and dash lines show tumor radius 16 mm.

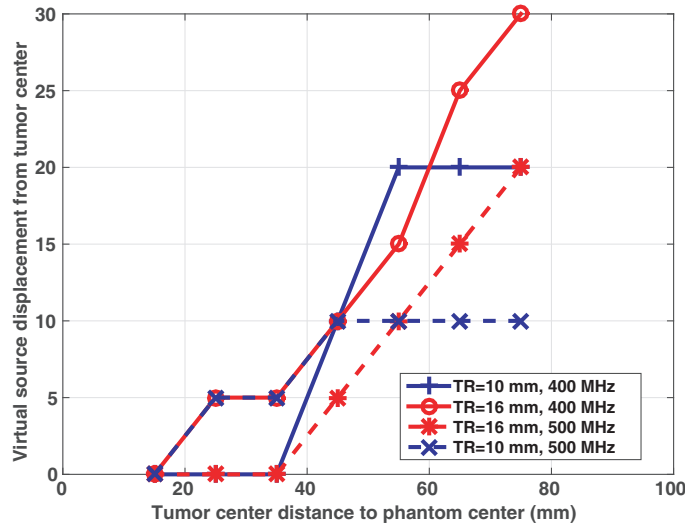


Figure 12. Virtual source displacement from tumor center to TC_{max} position at 400 MHz and 500 MHz versus the tumor center position.

was added below the chin to prevent unwanted wave reflections from the sharp boundary between the applicator and air. These reflections lead to extra hot spots in chin area and reduce the power which can absorb in the tumor. Figure 13(a) shows the applicator and the extra water bag in the mid-sagittal plane which goes through the tongue tumor. For simulations with the virtual source position in the tumor center using time-reversal analysis, the additional water bag resulted in 11% improvement in $TC_{25\%}$ and 91% improvement in $TC_{50\%}$ at 500 MHz. The tumor coverage values at 500 MHz was 46% for $TC_{50\%}$ and 98% for $TC_{25\%}$.

In order to find the optimum position of the virtual source, 7 positions were considered along the middle-z plane of the tongue tumor, see Figure 14. All time reversal analyses were performed at 500 MHz. The obtained aPA, RTMi and 25% tumor coverage versus virtual source positions are given in Table 3. The highest aPA and lowest RTMi were obtained at virtual source position 7, which is at the center of tumor. The worst aPA and RTMi values were obtained at virtual source positions 1 and 5, respectively. Computing $TC_{25\%}$ for all virtual source positions resulted in highest tumor coverage of 98% at tumor center, virtual source position 7.

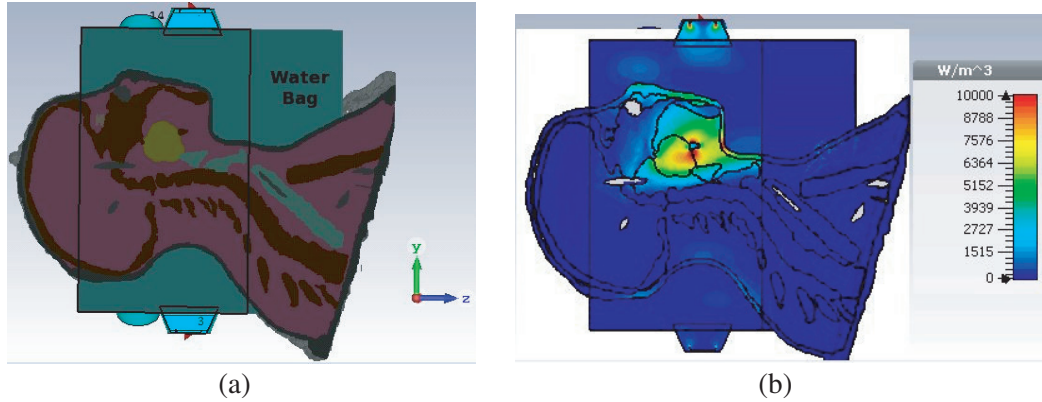


Figure 13. (a) The head applicator with an extra water bag. (b) Computed power loss distribution in the tongue tumor at 500 MHz.

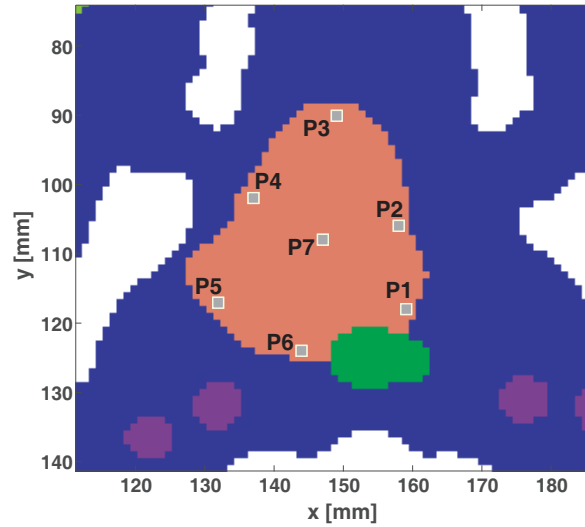


Figure 14. Positions of the virtual sources along the middle-z plane of the tongue tumor, pink area.

Table 3. Computed aPA, RTMi and TC_{25%} for virtual source positions in the tongue tumor.

	P_1	P_2	P_3	P_4	P_5	P_6	P_7
aPA	8.08	9.34	10.85	11.14	9.46	10.48	14.18
RTMi	1.98	1.48	1.51	1.64	2.26	1.3	1.01
TC _{25%}	53	56	44	25	46	65	98

4. DISCUSSION

In this paper we have presented a study of treatment planning for hyperthermia based on the time reversal method. The different studies presented in the paper can be divided in 2 parts. The results in Section 3.1 were related to finding the optimal frequency given the antenna system and tumor position. The results in Section 3.2 were related to optimizing the performance with respect to virtual source position in the treatment planning algorithm. Starting with results in Section 3.1, analytical results based on plane wave propagation were first presented. This was followed by a 2D numerical analysis.

In these studies the focusing ability was evaluated in terms of the aPA ratio and tumor coverage. The result of both studies indicate that for a superficial tumor, the highest aPA values were obtained using higher frequencies where aPA was improved with increasing the number of antennas. However for deep seated tumors, the highest aPA values were obtained for lower frequencies where we did not observe any strong benefit using more antennas. The optimum frequency range for hyperthermia treatment in terms of the number of antennas and the tumor position was summarized in Table 2.

In Section 3.2.1, we presented results on the optimum position of the virtual source in the time reversal method. First, a simple 3D model was used to find the optimum position of the virtual source for maximum tumor coverage. We considered different positions of the virtual source for each tumor position while we moved the tumor from the surface to the center of the phantom. We found that optimum performance in terms of high aPA and tumor coverage in this setup was obtained for frequency range 400–500 MHz, for all tumor positions. We then used $TC_{50\%}$ to assess the quality of the treatment for a virtual source position and a given position and size of the tumor. It was shown that at lower frequencies, the optimum virtual source position moves toward the phantom center as the tumor is moved toward the phantom surface. As we increased the frequency, the $TC_{50\%}$ got lower for deep seated tumors. At 900 MHz, $TC_{50\%}$ were negligible for all tumor positions.

In Section 3.2.2, results showed the optimum virtual source position in a realistic tumor model in 3D. For the tongue tumor used, we found that the optimum frequency range was 400–500 MHz. The obtained optimum virtual source position for the tongue tumor was in the tumor center which is in agreement with previous presented analysis using a spherical tumor inside a homogeneous elliptical phantom.

5. CONCLUSIONS

In this paper we investigated methods to improve the hyperthermia treatment quality by employing time reversal as the focusing technique. We presented a simple frequency selection scheme for tumor treatment, based on the tumor size, the position of the tumor and the number of antennas in the applicator. The suggested frequencies were used in treatment modeling of realistic tumor models and resulted in clinically acceptable hyperthermia quality indicators. We also presented a selection schemes to find the optimum virtual source position in the time reversal method. The analysis using simple tumor models agreed well with the results in more realistic tumor models.

REFERENCES

1. Cihoric, N., A. Tsikkinis, G. van Rhoon, H. Crezee, D. M. Aebbersold, S. Bodis, et al., "Hyperthermia-related clinical trials on cancer treatment within the ClinicalTrials.gov registry," *Int. J. Hyperthermia*, Vol. 31, No. 6, 609–614, 2015.
2. Datta, N. R., S. G. Ordonez, U. S. Gaipal, M. M. Paulides, H. Crezee, J. Gellermann, D. Marder, E. Puric, and S. Bodis, "Local hyperthermia combined with radiotherapy and/or chemotherapy: Recent advances and promises for the future," *Cancer Treat Rev.*, Vol. 41, No. 9, 742–753, Nov. 2015, doi: 10.1016/j.ctrv.2015.05.009, Epub 2015 May 27.
3. Lee, H. K., A. G. Antell, C. A. Perez, et al., "Superficial hyperthermia and irradiation for recurrent breast carcinoma of the chest wall: Prognostic factors in 196 tumors," *Int. J. Radiat. Oncol. Biol. Phys.*, Vol. 40, 365–375, 1998.
4. Franckena, M., D. Fatehi, M. de Bruijne, et al., "Hyperthermia dose-effect relationship in 420 patients with cervical cancer treated with combined radiotherapy and hyperthermia," *Eur. J. Cancer*, Vol. 45, No. 11, 1969–1978, Jul. 2009.
5. Turner, P. F., A. Tumeh, and T. Schaefermeyer, "BSD-2000 approach for deep local and regional hyperthermia: Physics and technology," *Strahlenther Onkol.*, Vol. 165, 738–741, 1989.
6. Crezee, J., P. M. A. van Haaren, H. Westendorp, M. de Greef, H. P. Kok, J. Wiersma, et al., "Improving locoregional hyperthermia delivery using the 3-D controlled AMC-8 phased array hyperthermia system: A preclinical study," *Int. J. Hyperth.*, Vol. 25, 581–592, 2009.

7. Paulides, M. M., J. F. Bakker, E. Neufeld, J. van der Zee, P. P. Jansen, P. C. Levendag, and G. C. van Rhooon, "The HYPERcollar: A novel applicator for hyperthermia in the head and neck," *Int. J. Hyperth.*, Vol. 23, 567–576, 2007.
8. Togni, P., Z. Rijnen, W. C. Numan, R. F. Verhaart, J. F. Bakker, G. C. van Rhooon, and M. M. Paulides, "Electromagnetic redesign of the HYPERcollar applicator: Toward improved deep local head-and-neck hyperthermia," *Phys. Med. Biol.*, Vol. 58, No. 17, 5997–6009, 2013.
9. Dobšiček Trefná, H., J. Vrba, and M. Persson, "Time-reversal focusing in microwave hyperthermia for deep-seated tumors," *Phys. Med. Biol.*, Vol. 55, No. 8, Apr. 2010.
10. Converse, M., E. J. Bond, B. D. Van Veen, and S. C. Hagness, "A computational study of ultra-wideband versus narrowband microwave hyperthermia for breast cancer treatment," *IEEE Transactions on Microwave Theory and Techniques*, Vol. 54, No. 5, 2169–2180, 2006.
11. Dobšiček Trefná, H., P. Togni, R. Shiee, J. Vrba, and M. Persson, "Design of a wide-band multi-channel system for time reversal hyperthermia," *Int. J. Hyperthermia.*, Vol. 28, No. 2, 175, 2012.
12. Dobšiček Trefná, H., M. Shafiemehr, and M. Persson, "Laboratory prototype of UWB applicator for head and neck hyperthermia," *12th International Congress on Hyperthermic Oncology ICHO 2016*, New Orleans, USA, Apr. 11–15, 2016.
13. Paulides, M. M., R. R. Stauffer, E. Neufeld, P. F. Maccarini, A. Kyriakou, R. A. M. Canters, C. J. Diederich, J. F. Bakker, and G. C. Van Rhooon, "Simulation techniques in hyperthermia treatment planning," *Int. J. Hyperthermia.*, Vol. 29, No. 4, 346–357, 2013.
14. Kok, H. P., P. Wust, P. R. Stauffer, F. Bardati, G. C. van Rhooon, and J. Crezee, "Current state of the art of regional hyperthermia treatment planning: A review," *Radiat. Oncol.*, Vol. 10, 196, 2015.
15. CST, Computer Simulation Technology, Retrieved from <https://www.cst.com/Products/CSTMWS>.
16. Dobšiček Trefná, H., M. Shafiemehr, and M. Persson, "Laboratory prototype of UWB applicator for head and neck hyperthermia," *12th International Congress on Hyperthermic Oncology ICHO 2016*, New Orleans, USA, Apr. 11–15, 2016.
17. Gabriel, S. R. W. Lau, and C. Gabriel, "The dielectric properties of biological tissues: III. Parametric models for the dielectric spectrum of tissues," *Phys. Med. Biol.*, Vol. 41, 2271–2293, 1996.
18. Lazebnik, M., L. McCartney, D. Popovic, C. B. Watkins, M. J. Lindstrom, J. Harter, S. Sewall, A. Magliocco, J. H. Booske, M. Okoniewski, and S. C. Hagness, "A large-scale study of the ultra-wideband microwave dielectric properties of normal breast tissue obtained from reduction surgeries," *Phys. Med. Biol.*, Vol. 52, 2637–2656, 2007.
19. Canters, R. A. M., P. Wust, J. F. Bakker, and G. C. Van Rhooon, "A literature survey on indicators for characterization and optimization of SAR distributions in deep hyperthermia, a plea for standardization," *Int. J. Hyperthe.*, Vol. 25, No. 7, 593–608, 2009.